SCIENCE CHINA
Technological Sciences

• Review •

October 2016 Vol.59 No.10: 1537–1548
doi: 10.1007/s11431-015-0999-6

A novel technique for probing phase transitions in ferroelectric functional materials: Condensed matter spectroscopy

ZHANG JinZhong, JIANG Kai, HU ZhiGao* & CHU JunHao

Department of Electronic Engineering, East China Normal University, Shanghai 200241, China

Received December 23, 2015; accepted June 19, 2016; published online September 14, 2016

As relaxor ferroelectric functional materials, their crystal structures depend on temperature, component, electric filed, pressure, and so on, which are important for the applications of sensors, transducers, and actuators. For the case of $PbTiO_3$-based ferroelectrics $Pb(Zn_{1/3}Nb_{2/3})O_3$-$PbTiO_3$, $Pb(Mg_{1/3}Nb_{2/3})O_3$-$PbTiO_3$, $Pb(In_{1/2}Nb_{1/2})O_3$-$Pb(Mg_{1/3}Nb_{2/3})O_3$-$PbTiO_3$ and some other crystals, they have been extensively investigated due to the excellent electromechanical and piezoelectric properties. Generally, ferroelectric crystal structure and corresponding phase diagram are detected by temperature-dependent high resolution X-ray diffraction, low frequency dielectric permittivity, and domain structures. In this review, we focus on the novel condensed matter spectroscopy (i.e., spectroscopic ellipsometry, transmittance, photoluminescence spectra as well as Raman spectra), which is nondestructive, noncontact, and sensitive optical techniques for probing symmetries, phase transitions and phase diagrams of ferroelectric crystals. Besides, it can supply some other physical and chemical information for ferroelectric and semiconductor functional materials such as optical band gap, electronic transitions, dielectric functions, optical conductivity, absorption, phonon modes, lattice dynamics as functions of temperature and PT composition.

ferroelectrics, phase diagram, Raman scattering, ellipsometric spectroscopy, transmittance, photoluminescence

Citation: Zhang J Z, Jiang K, Hu Z G, et al. A novel technique for probing phase transitions in ferroelectric functional materials: Condensed matter spectroscopy. Sci China Tech Sci, 2016, 59: 1537–1548, doi: 10.1007/s11431-015-0999-6

1 Introduction

Recently, perovskite ferroelectric functional materials have attracted considerable attention and intensive research from the viewpoint of excellent ferroelectric and piezoelectric properties for the understanding of fundamental physics and applications in multifunction devices [1–7]. In particular, $PbTiO_3$ (PT)-based perovskite ferroelectric materials, such as $Pb(Zn_{1/3}Nb_{2/3})O_3$-$x$$PbTiO_3$ (PZN-xPT), $Pb(Mg_{1/3}Nb_{2/3})O_3$-$x$$PbTiO_3$ (PMN-xPT), and $(1–x–y)Pb(In_{1/2}Nb_{1/3})O_3$-$y$$Pb(Mg_{1/3}Nb_{2/3})O_3$-$x$$PbTiO_3$ (PIN-yPMN-xPT), have been widely investigated due to their excellent piezoelectric coefficient, strain levels reaching induced by electric field, and a high electromechanical coupling coefficient especially for the PT composition near a mophotronic phase boundary (MPB), which are essential for the technological applications of ultrasonic transducers, solid actuators, and sonar [8–15]. The MPB is a phase boundary, which separates different crystal structures in a phase diagram. For PZN-xPT and PMN-xPT functional materials at room temperature, it corresponds to x~8%–10% and x~26%–39%, respectively [16,17]. Accurately, the MPB separates the ferroelectric rhombohedral phase and ferroelectric tetragonal one in the phase diagram of PZN-xPT (PMN-xPT) [18,19]. A schematic phase diagram and related polarization-rotation path of the PT-based relaxor ferroelectrics (PZN-xPT, PMN-xPT, (1-x-y)PIN-yPMN-xPT, etc.) are shown in Figure 1 [3]. Generally, the crystal structure is cubic (C) symmetry above

*Corresponding author (email: zghu@ee.ecnu.edu.cn)

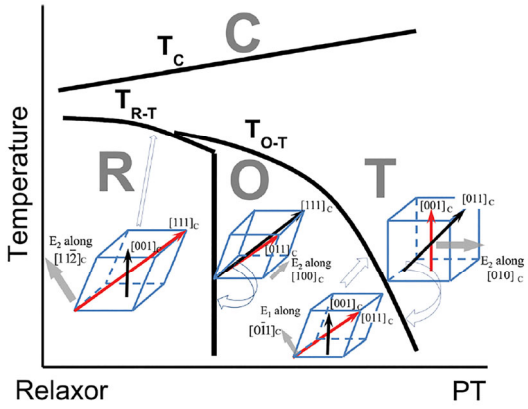

Figure 1 (Color online) A schematic phase diagram and polarization rotations for PT-based relaxor ferroelectric crystals [3].

the Curie temperature (T_C). On the other hand, there are different symmetries including rhombohedral (R), orthorhombic (O), and tetragonal (T) phases in different temperature regions and PT compositions below T_C. It should be noted that the O phase is used instead of the monoclinic (M) phase since the M phase is a slightly distorted O phase. According to the phase diagram, PT-based ferroelectrics with the x composition below MPB undergo R-T-C phase transitions. While above MPB, they have a T→C phase transition upon heating [1,15–18]. Moreover, it is reported that PZN-xPT crystals with the PT composition near MPB exhibit excellent optical properties. For example, PZN-8%PT has a relative large electro-optic (~450 pm/V poled along [001] direction) and photoelastic coefficient (~19×10^{-12} m^2/N), which are expected to be applied in various linear and nonlinear optical devices [20,21].

Usually, crystal structures and phase diagrams can be identified by traditional techniques: X-ray diffraction based on the various trends of lattice constants (a, b, and c) and angles (α, β, and γ) as a function of temperature [18,22,23]; For ferroelectrics, temperature dependence of dielectric permittivity in the low frequency region below 10^6 Hz is an effective method to detect phase transitions especially Curie temperature, which is the phase transition between ferroelectric and paraelectric phases [24–29]; Polarizing light microscopy also can detect phase transitions according to various domain structures at different temperatures [30–32]. In addition, there are some other techniques such as neutron diffraction, transmission electron microscope (TEM), birefringence imaging measurements for probing phase transitions and phase diagrams [16,17,33]. However, there are some disadvantages of traditional techniques as following: 1) X-ray diffraction cannot supply more physical properties (optical, electric, and thermal properties) besides that of crystal structures; 2) low frequency electric measurements are contact type with electrodes, which are often complicated and hindered by parasitic charges forming at interface and electrodes; 3) sample preparation of TEM is very expensive. Compared to the traditional techniques (X-ray diffraction, low frequency electric measurements, TEM, etc.), the novel condensed matter spectroscopy is nondestructive, noncontact, and sensitive for probing phase diagrams, and can supply more information of physical and chemical properties such as temperature response of optical band gap, electronic transitions, optical constants, absorption, phonon modes, lattice dynamics [34–46]. As a condensed matter spectroscopy, Raman scattering is an effective technique to study ferroelectric phase transitions base on the various trends of peak position, integrated intensity, and bandwidth of first-order Raman modes on heating or cooling [34–40]. Besides, some other optical methods such as spectroscopic ellipsometry (SE), transmittance, photoluminescence (PL), and infrared spectra, are used to probe ferroelectric phase transitions and phase diagrams [41–46].

The review is organized as follows: Section 2 presents the traditional techniques (X-ray diffraction, low frequency dielectric permittivity, polarizing light microscopy, etc.) to obtain ferroelectric crystal structures and phase diagrams below and above room temperature. For the case of $PbTiO_3$-base functional ferroelectrics, temperature dependent condensed matter spectroscopy, which is related to phase transitions and diagrams as well as optical properties, are described in detail in Section 3. Finally, conclusion and prospect are drawn in Section 4.

2 Traditional techniques

2.1 Temperature-dependent X-ray diffraction

X-ray diffraction (XRD) is a rapid and nondestructive tool for structure characterization of functional materials [47–49]. For ferroelectrics, it can be used to determine lattice parameters, crystal symmetries, expansion tensors, phase transitions, etc. [22,23,38]. The 25%PIN-42%PMN-33%PT crystals are grown from the melt by a modified Bridgman method [4,50] and its pseudo-cubic (002) and (220) diffraction peaks at the zero-filed-cooling (ZFC) and zero-field- heating (ZFH) conditions have been investigated in detail (not shown) [4]. At high temperature above 190°C, the C phase is stable since a single sharp peak is observed. A transition from C phase to T phase appears on cooling to 180°C due to an additional peak at lower scattering angle. On further cooling to 140°C, a coexistence of C and T is observed due to the tetragonal (002)-(200) doublet and residual cubic (002) singlet. Finally, the broad rhombohedral (002) singlet appears at the temperature below 110°C. In addition, it has the same phase transitions (R-T-C) upon heating [4]. Based on the XRD patterns of 25%PIN-42%PMN-33%PT crystals, the lattice parameters and angles have various trends on cooling/heating without applying electric filed as shown in Figure 2. It indicates that 25%PIN-42%PMN-33%PT undergoes R-T-C transitions.

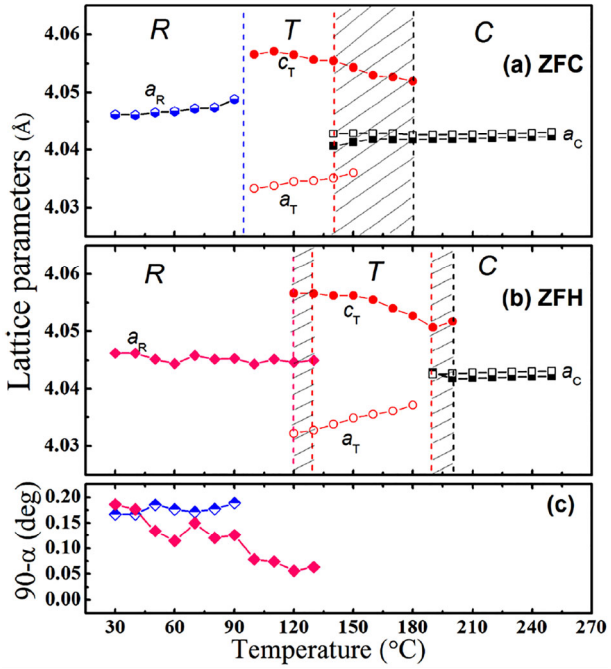

Figure 2 (Color online) Lattice parameters of 25%PIN-42%PMN-33%PT crystals for (a) ZFC and (b) ZFH processes, and (c) the tilt angles for *R* phase. Note that the open squares are obtained from $(220)_C$ diffraction data and the solid ones are obtained from the $(002)_C$ peaks at high temperature [4].

Note that the shadow regions indicate the coexistence of adjacent two phases and the phase-transition temperatures derived by cooling and heating have a deviation since the crystal structure exhibits thermal hysteresis. Therefore, the temperature-dependent XRD can determine ferroelectric phase transitions rapidly and nondestructively. Unfortunately, the disadvantages of XRD are that it cannot supply more information about other chemical and physical properties (lattice dynamics, optical constants, absorption, band gap, etc).

2.2 Dielectric permittivity in a low frequency region

In the frequency region of 10–10^6 Hz, temperature dependent dielectric permittivity of dielectric materials can be determined by using a LCR meter equipped with a temperature chamber [48–50]. For example, Figure 3(a) shows the temperature-dependent dielectric permittivity of PMN-32%PT relaxor ferroelectric at some typical frequencies [25]. Obviously, there are two peaks upon heating. The first one near 379 K indicates the ferroelectric R to ferroelectric T phase transition. The other one (T_m) near 410 K corresponds to the phase transition from ferroelectric T phase to paraelectric C phase. It should be emphasized that the second peak becomes broadening and weak with increasing frequency. It indicates the relaxor behavior of diffuse phase transitions, which is consistent with other PT-based relaxor ferroelectrics [50,51]. For a further step to understand the relationship between phase transitions and dielectric permittivity, the dielectric behavior at the temperature above T_m was characterized by the Curie-Weiss law: $\varepsilon'(T)=A/(T-T_{CW})$ [25]. Here the parameter A is the Curie-Weiss constant and T_{CW} is the Curie-Weiss temperature. The corresponding fitting results of inverse dielectric permittivity $1/\varepsilon'$ as a function of temperature at 10 kHz are show in Figure 3(b). There are three characteristic temperatures of about 410 K (T_m), 453 K (T_{CW}), and 514 K (T_B). Note that T_B denotes the Burns temperature from which dielectric behavior follows the Curie-Weiss law. Moreover, the dielectric behavior in the temperature region between T_m and T_B follows the empirical Lorentz type relation: $\varepsilon'(T)=2\delta^2\varepsilon_A/[(T-T_A)^2+2\delta^2]$, where ε_A and T_A are the fitting parameters, and δ denotes the diffuseness of permittivity peak. Therefore, the temperature-dependent dielectric permittivity can characterize ferroelectric phase transitions directly. However, a disadvantage is that phase transition temperatures are less accurate because the external influence from the interface and electrodes cannot be avoided.

2.3 Temperature-dependent domain structure

In poled ferroelectric materials, domain structures are related to various crystal structures [52–54]. As shown in Figure 1, the polarization direction is deviation in different symmetries and it will rotate by applying electric field [3]. The

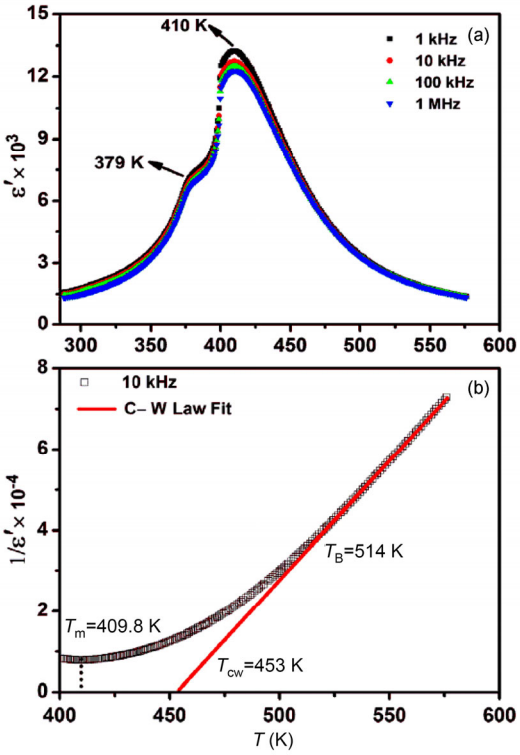

Figure 3 (Color online) (a) Temperature-dependent dielectric permittivity of PMN-32%PT single crystals at different frequencies; (b) the experimental (dotted line) and Curie-Weiss law fitting (solid line) $1/\varepsilon'$ as a function of temperature at 10 kHz [25].

observation of domain configurations using polarizing light microscopy is based on the birefringence of the crystal. Taking the $[011]_C$ poled PMN-0.33PT single crystal as an example, its phase transition sequence and domain configuration evolution on heating and cooling have been investigated in detail [33].

Figure 4 shows the polarizing light microscopy of PMN-0.33PT single crystal and corresponding crystal symmetries are inferred based on the extinction position and orientation of domains. Accurately, during heating process, the structure is a mixture of M_A and O phases at room temperature as shown in Figure 4(a). On heating, the sample becomes less transparent (Figure 4(b)) and then complete extinction at 45° (Figure 4(c)), while transparent at 0° (Figure 4(d)). The single domain configuration of O or R phase can explain the phenomenon. Therefore, the crystal structure belongs to R phase until 93°C, at which R domains disintegrated dramatically and a new phase (M_C) was observed as shown in Figure 4(e) and (f). When the temperature further increases till 155°C, another dramatic change (extinction) of domain structure appears (Figure 4(g)) and its inset indicates the formation of C phase with a small fraction of R phase nanodomain clusters. Finally, the remaining R phase cluster changes into the C phase upon further heating as shown in Figure 4(i) and (j). Therefore, the $[011]_C$ poled PMN-0.33PT crystal has a serious phase transitions (M_A+O→R→M_C→C phases) upon heating. On the other hand, the right-hand two columns III and IV of Figure 4 show the domain structure at various temperatures on cooling. It suggests that the crystal belongs to C phase in the temperature region above 141°C (Figure 4(i) and (ii)). On

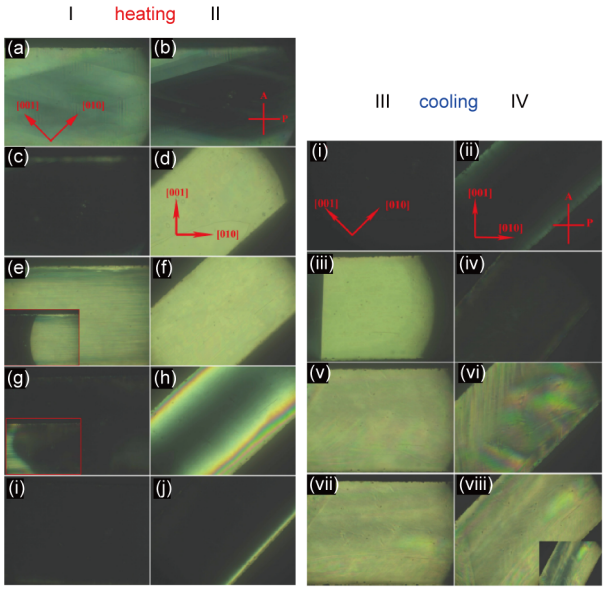

Figure 4 Columns I and II: domain structures of PMN-0.33PT crystal observed at various temperatures on heating at (a) 30°C; (b) 40°C; (c,d) 55°C; (e,f) 93°C; (g,h) 155°C; and (i,j) 170°C. Column I corresponds to θ=45°and II corresponds to θ=0°. Column III and IV: domain structures observed on cooling at (i,ii) 150°C; (iii,iv) 141°C; (v,vi) 68°C; and (vii, viii) 30°C. Column III corresponds to θ=45° and IV corresponds to θ=0° [32].

further cooling till 48°C, dramatic domain changes as shown in Figure 4(iii) and 6(iv) and a new phase (T) appears because of extinction at 0° and transparency at 45°. And then another phase (M_A) occurs based on the abrupt changes of domain structure and there is no more phase on further cooling (Figure 4(v)–(viii)). Therefore, the crystal undergoes the structure transitions from C→T→M_A phases on cooling. In summary, upon heating, it goes through the phase transitions from the M_A and O mixture phase to R phase at 55°C, to M_C phase at 93°C, and finally to C phase at 155°C. On the other hand, the crystal is transformed from C to T phase at 141°C and M_A phase at 68°C on cooling [33]. Therefore, the high sensitivity of the polarized light transmission intensity to the orientation of the optical indicatrix makes optical microscopy a powerful tool to study the crystal symmetry and phase transition sequence according to the various domain structures. However, the limitation of the techniques is that it most commonly used on birefringent samples and the plate samples should been thinned in order to reduce the overlap of domains along the observing direction [32].

3 Novel spectroscopic techniques

To avoid the disadvantages of traditional techniques for investigating ferroelectrics, some novel condensed matter spectroscopic techniques (Raman scattering, SE, transmittance, as well as PL spectra) are used for probing ferroelectric phase transitions and diagrams based on optical band gap, electronic transitions, optical constants, Raman- and infrared-active phonons, and other physical parameters [55–69].

3.1 Raman spectroscopy

Raman and infrared spectra are usually used in condensed matter and material physics and chemistry since vibrational information is specific to the lattice dynamics, symmetries, and chemical bonds. It can provide a fingerprint by which crystal structures and moleculars can be identified [70–73]. For examples, the temperature-dependent polarized Raman scatterings of PZN-7%PT, 27%PIN-40% PMN-33%PT, and 95%$(K_{0.5}Na_{0.5})NbO_3$-5%$LiNbO_3$ (KNN-5%LN) ferroelectric single crystals have been investigated in detail as following [34,72,73].

Figure 5 shows the polarized Raman spectra of the <001>-orient PZN-7%PT crystal with various temperatures in the VV (the polarizer and analyzer in vertical position) and VH (the polarizer in vertical position and the analyzer in horizontal position) scattering geometries. It should be emphasized that all measured Raman spectra were divided by the Bose-Einstein occupation number $n+1=1/[1-\exp(-\hbar\omega/k_BT)]$ to get rid of trivial temperature dependence. Here $\hbar$ and k_B are Planck and Boltzmann constants, respec-

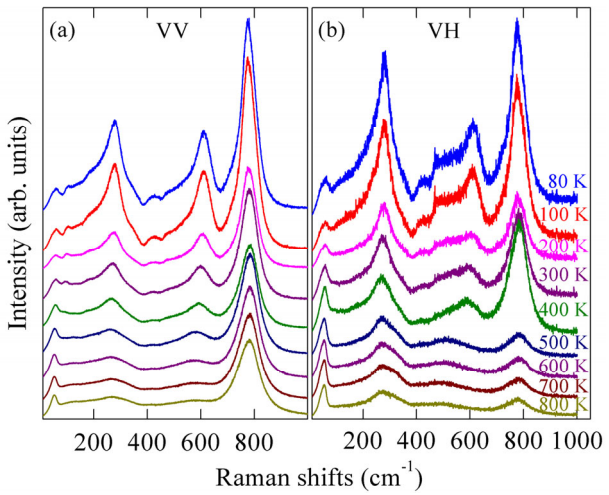

Figure 5 (Color online) (a) VV and (b) VH polarized Raman spectra of the PZN-7%PT single crystal at different temperatures. Note that each spectrum is shifted in intensity for clarity [72].

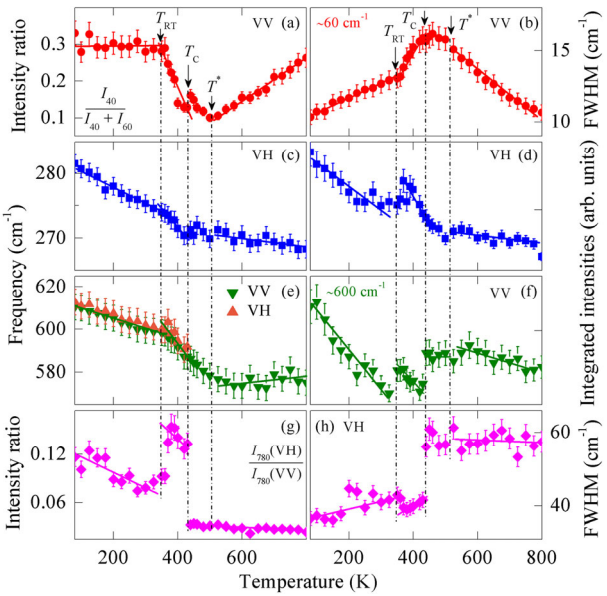

Figure 6 (Color online) Temperature dependence of (a) integrated intensity ratio $I_{40}/(I_{40}+I_{60})$ and (b) FWHM of ~60 cm^{-1} in the VV geometry; (c) peak positions and (d) FWHM of ~270 cm^{-1} in the VH geometry; (e) peak positions in the VV and VH geometries; and (f) FWHM in the VV geometry of the mode near 600 cm^{-1}; (g) integrated intensity ratio I_{780}(VH)/I_{780}(VV) between VH and VV geometries and (h) FWHM in the VH geometry of the mode near 780 cm^{-1} [72].

tively [74]. Upon heating, the polarized Raman spectra have a similar shape except that the intensity of the band near 780 cm^{-1} has a dramatic decrease in the VH geometry compared to that in VV one. Moreover, the band located at about 600 cm^{-1} in the VH scattering geometry vanishes on further heating. These phenomena suggest that the crystal structure of PZN-7%PT changes and there are phase transitions in the temperature region of 300–600 K [72].

The peak positions, integrated intensity, and linewidths (full width at half maxima, FWHM) of Raman modes for PZN-7%PT crystals are obtained by fitting the polarized Raman spectra with muti-Lorentzan functions. Some typical simulation results are shown in Figure 6. Accurately, the two bands near 50 cm^{-1} origin from Pb localized modes. The lower one origins from the Pb1 surrounded by Nb^{5+} ions, which reflects the ferroelectric long-range order. On the other hand, the higher one arises from the Pb2 surrounded by Zn^{2+} and Nb^{5+} ions. The phase transition (R→T→C) temperatures as well as an intermediate temperature are successfully extracted based on the various trends of integrated intensity and FWHM with increasing the temperature (Figure 6(a) and (b)). The results can be confirmed by some other first-order Raman-active modes as shown in Finger 6(c)–(h). Theoretically, the mode near 270 cm^{-1} arises from vibrations of off-centered B-site cations. It is sensitive to the development of polar order, which is related to the coupling processes at the intermediate temperature [75]. Moreover, the one at about 600 cm^{-1} is related to oxygen bending vibration [76]. Obviously, the peak near 780 cm^{-1} is strong and its physical parameters can be obtained very well. This mode can effectively reflect the subtle changes in the lattice structure [77]. Based on the temperature-dependent polarized Raman-active mode behaviors, the PZN-7%PT ferroelectric crystal undergoes two phase transitions from ferroelectric R to ferroelectric T phases and from ferroelectric T to paraelectric C phases at 360 and 440 K, respectively, as well as an intermediate temperature (T*~510 K) upon heating [72].

Moreover, the phase transitions of 27%PIN-40%PMN-33%PT crystals can also be observed by the intensity of polarized Raman-active modes with increasing temperature as shown in Figure 7. The dotted lines show the respective transition temperatures, including the coexistence of multiple (R, M, and O) phases →R phase transition at 325 K, R →T phase transition at 390 K, and T →C phase transition (T_C) at 460 K. In addition, the phase transitions (O→O+T→T→C) of KNN-5%LN can also be observed by the frequency trends of Raman modes on heating in the temperature region of 300–800 K [34]. Therefore, the temperature-dependent Raman spectroscopy is a useful technique to detect phase transitions of functional ferroelectrics directly and nondestructively according to the various trends of peak positions, intensity, and bandwidth as a function of temperature. However, a limitation is that it is difficult to identify the assignments of first-order Raman modes due to the peak overlaps and second-order modes, which will decrease the accuracy of analysis.

3.2 Ellipsometric spectroscopy

Based on the reflectance configuration, SE is an effective tool to extract simultaneously thickness and optical constants of a multilayer system [78–83]. It is a nondestructive

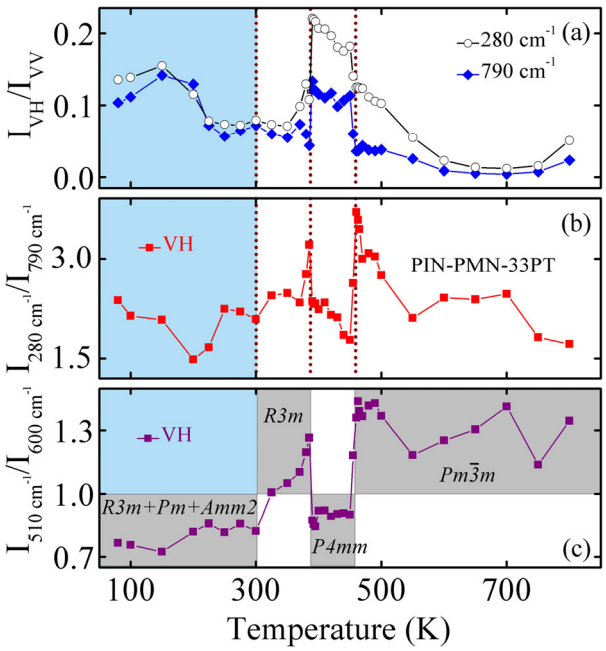

Figure 7 (Color online) Temperature dependence of (a) the intensity ratio of the modes near 280 and 790 cm^{-1}, and the intensity ratio between the modes (b) 280 and 790 cm^{-1}; (c) 510 and 600 cm^{-1} in the VH geometry for 27%PIN-40%PMN-33%PT crystal [73].

and sensitive optical technique, which measures the relative changes in the amplitude and phase of particular directions for polarized lights upon oblique reflection from the sample surface [72]. The physical parameters measured by ellipsometry are the complex ratio $\rho(E)$ in terms of $\Psi(E)$ and $\Delta(E)$, which are defined by the formula $\rho \equiv r_p/r_s = \tan\Psi e^{i\Delta}$, here, r_p and r_s are the complex Fresnel's reflection coefficient of the light polarized parallel and perpendicular to the incidence plane, respectively. The ellipsometric parameters Ψ and Δ are related to photon energy E, incident angle θ, thickness d, and dielectric functions $\varepsilon(E)$ of measured materials [72,83]. For bulk materials with idealized smooth surface, the dielectric functions can be calculated directly [84]:

$$\langle\varepsilon\rangle = \langle\varepsilon'\rangle + i\langle\varepsilon''\rangle = \sin^2\theta[1+\tan^2\theta(1-\rho)^2/(1+\rho)^2]. \quad (1)$$

Correspondingly, the complex refractive index $\boldsymbol{N}(E)$ can be derived according to the relationship between $N(E)$ and $\varepsilon(E)$ ($\boldsymbol{N}=n-ik=\varepsilon^{1/2}$). Actually, an appropriate model has to be assumed for a bulk material with a rough surface [72]. For the case of a multilayer structure (air/surface roughness layer/bulk material), dielectric functions of each layer should be obtained by fitting experimental SE spectra with an appropriate dielectric mode based on the Fresnel equation, Snell's law, and the light absorption at layer surface [79–84]. Usually, the optical constants of air is unit (refractive index n=1) without absorption (extinction coefficient k=0). For the case of relaxor-based crystals, dielectric functions of the surface roughness layer can be described by the Bruggeman effective medium approximation ε_{eff} with the assumption 50% void component ε_v and 50% PT-based bulk crystal $\varepsilon_{\text{Bulk}}$ [0=0.5($\varepsilon_v-\varepsilon_{\text{eff}}$)/($\varepsilon_v-2\varepsilon_{\text{eff}}$)+0.5($\varepsilon_{\text{Bulk}}-\varepsilon_{\text{eff}}$)/($\varepsilon_{\text{Bulk}}-2\varepsilon_{\text{eff}}$)] [85]. Additionally, the dielectric response of crystals can be evaluated by the standard critical point model as following [86]: $\varepsilon_{\text{Bulk}}=A_1-A_2e^{i\phi}(E-E_k+i\Gamma)^{1/2}$, where the parameter A_1 is a constant. Therefore, a critical point is described by the parameters amplitude A_2, excitonic phase angle ϕ, electronic transition E_k, and broadening Γ. Correspondingly, the second partial derivation for showing electronic transitions in dielectric functions can be written as

$$\partial^2\varepsilon_{\text{Bulk}}/\partial E^2 = A_3e^{i\phi}(E-E_k+i\Gamma)^{-3/2}, \quad (2)$$

here the parameter A_3 is a constant. In order to investigate the intrinsic relationship between optical response and phase transitions of relaxor ferroelectrics, PIMN-xPT, PZN-xPT and other crystals around MPB have been studied by temperature-dependent ellipsometric spectra [64,72,78].

Figure 8(a) and (b) show the temperature-dependent ellipsometric spectra Ψ and Δ of PIMN-0.33PT crystals, respectively. It suggests that there are two gaps in the original experimental spectra at the temperatures of about 380 and 450 K, which indicates structure changes. Figure 8(c) illustrates the experimental measured at 200 and 400 K and corresponding fitting ellipsometric spectra with a three phase structure (air/surface roughness/crystal). The corresponding dielectric functions are shown in figure 8(d). It suggests that the optical band gap (E_g) is about 3.5 eV. At the energy region below E_g, it is transparent due to the lower value ε''. Electronic transitions appear above E_g according to the increasing of ε''. The relationship between ε' and ε'' follows Kramer-Kroning transformation. Moreover, the thickness of surface roughness is about 8±3 nm [78].

To understand the physical mechanism of electronic transitions for PT-based relaxor ferroelectrics, first- principles calculations of bulk PT are performed with the plane-wave pseudopotential calculations based on DFT to elucidate the origins of the critical point features, at the level of the local density approximation (LDA). The cutoff kinetic energy is 380 eV for the cubic perovskite structure of PT and the corresponding lattice constant is 0.397 nm. The calculated band structure and corresponding density of states are shown in Figure 9(a) and (b), respectively. As a matter of fact, the top of valance bands and bottom of conduction bands at the X point consist mainly O-2p and Ti-3d states, respectively. The direct band pap is about 1.64 eV, which is smaller than the experimental gap due to the well-know LDA band-gap error. Moreover, the higher conduction bands originate from mainly Pb-6p and Ti-3d states. On the other hand, the valance bands near –7 eV consist of mainly Pb-6s states. These phenomena are consistent with other results [87].

According to physical mechanism of the Bruggeman effective medium approximation and the standard critical point dielectric function model, electronic transitions de-

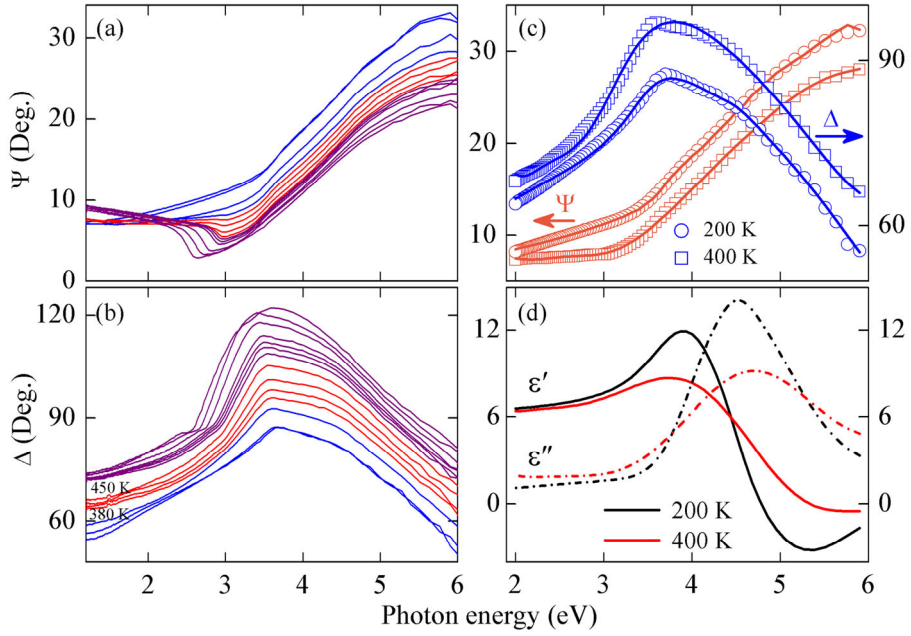

Figure 8 (Color online) Temperature dependence of experimental (a) Ψ and (b) Δ spectra for a PIMN-0.33PT single crystal; (c) the experimental (dotted lines) and fitting (solid lines) Ψ and Δ spectra at 200 and 400 K; (d) the real part (ε') and imaginary part (ε'') of numerically inverted complex dielectric functions at 200 and 400 K [78].

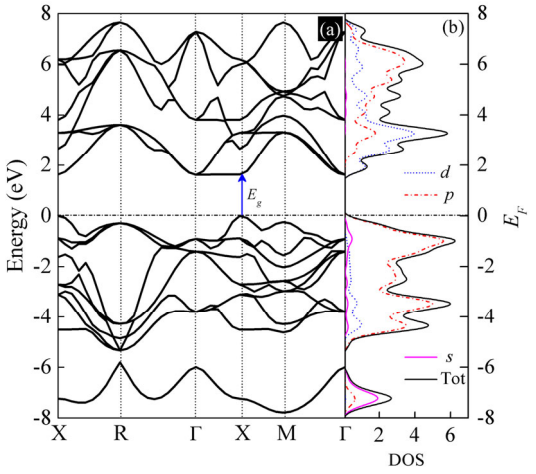

Figure 9 (Color online) (a) Calculated band structure and (b) corresponding partial and total density of states for cubic $PbTiO_3$.

rived from eq. (2) are independent of the roughness surface, which affects related dielectric constant. Therefore, the simulation results of electronic transitions and other basic physical parameters for PIMN-*x*PT crystals have been also extracted by fitting the second partial derivation dielectric spectra $\partial\langle\varepsilon'\rangle^2/\partial E^2$ and $\partial\langle\varepsilon''\rangle^2/\partial E^2$, and the extracted temperature-dependent electronic transition energy (E_a, E_b, E_c, and E_d) with different PT compositions were plotted in Figure 10 [78]. Theoretically, E_a comes from the electronic transition from O-2p to Ti-d states since there is no E_a transition in the low temperature region (*R* phase) and the electronic transitions from O-2p (Pb-s) states to Nb-d ones have larger contribution to E_b. Moreover, the higher electronic transition E_c comes from the O-2p/Pb-s to Pb-p states. The other one E_d is probably derived from the weak Ti/Nb-O hybridization induced by coexistence of multiphase in the MPB region [78,88]. Figure 10 suggests various trends of the four electronic transitions as a function of temperature in PIMN-*x*PT crystals with different PT compositions. According to the temperature response, there are some phase transitions with increasing the temperature. For the case of PIMN-0.33PT crystal upon heating as shown in Figure 10(c), the temperature of 380 K, at which E_d disappears while E_a appears, is taken as an assignment to determine the phase transition from M_C to T phases. Another transition from T to C phases is found at about 455 K according to the slope changes of E_a, E_b, and E_c.

Based on the temperature response of electronic transitions E_a, E_b, E_c, and E_d, a schematic phase diagram (solid lines) of PIMN-*x*PT single crystals is shown in Figure 11 [78,89]. It indicates that the R phase locates at the low PT composition side, while the T phase locates at the other side. And the MPB region locates in the PT composition region from 32% to 34%, which separates the R and T phase regions. The results derived from the temperature-dependent SE technique are consistent well with some other previous results (dashed lines) derived by temperature-dependent XRD and dielectric constant at low frequency region from 10^2 to 10^5 Hz [89,90].

In addition, the phase transition process of PZN-7%PT single crystal is also observed by the ellipsometric spectra based on the temperature dependence of the electronic transitions hv_1, hv_2 and hv_3, which are derived by fitting the se-

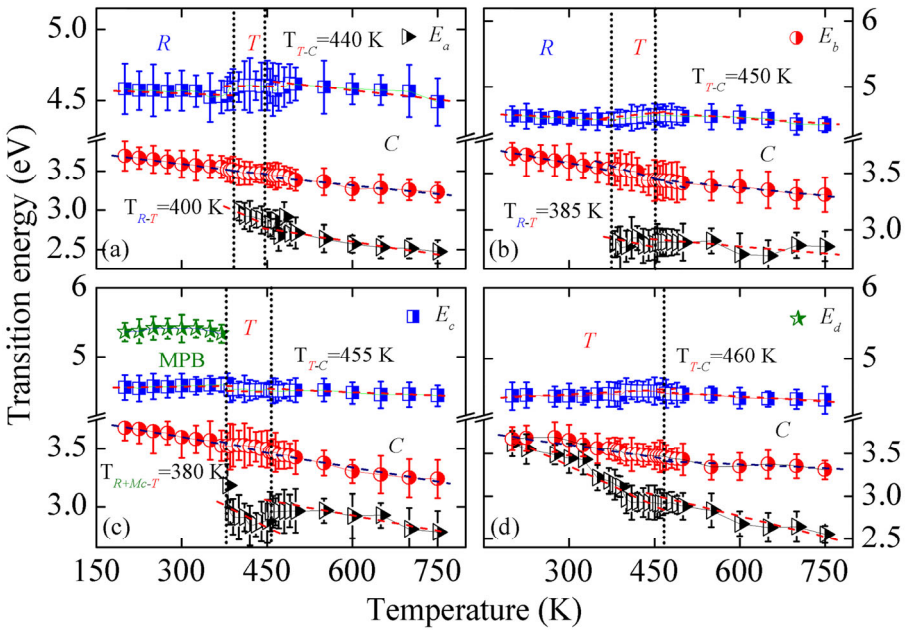

Figure 10 (Color online) Temperature dependence of the interband critical point energies (E_a, E_b, E_c, and E_d) for (a) PIMN-0.29PT, (b) PIMN-0.31PT, (c) PIMN-0.33PT, and (d) PIMN-0.35PT crystals, respectively. The dot lines are applied to guide the eyes and indicate anomaly behavior [78].

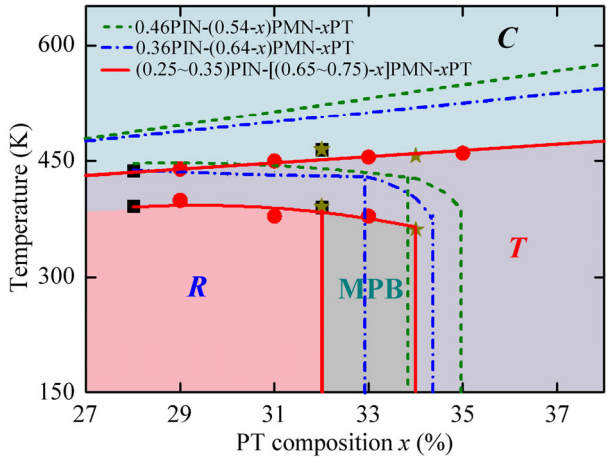

Figure 11 (Color online) A schematic phase diagram of PINM-*x*PT crystals. The solid lines indicate the phase transition boundary derived from the SE technique [78] and the dashed lines were taken from previous study [89].

cond partial derivatives of experimental pseudodielectric functions $\partial\langle\varepsilon\rangle^2/\partial E^2$ with the three phase structure and standard critical point models as shown in Figure 12 [72]. Accurately, the crystal has a phase transition sequence from *R* to T to C phases at 360 and 440 K upon heating, and the results are consistent with that observed by XRD and other traditional techniques. Therefore, the variable temperature ellipsometry is another effective technique for probing ferroelectric phase transitions and it can supply much more optical properties of film/bulk materials simultaneously. However, it not suitable for investigating powder materials.

3.3 Transmittance spectroscopy

As we know, the absorption coefficient α of functional materials can be characterized by transmittance spectra T based on the Beer's law: $T=I/I_0=e^{-\alpha d}$, here I and I_0 are the intensity of normal incident and transmitted light, respectively. And the parameter d is sample thickness. The material may absorb one color without others since α is a function of incident light frequency. Figure 13 shows the temperature dependence of transmittance spectra of PMN-0.12PT bulk crystals [91]. It suggests that the absorption edge located at about 400 nm presents a typical red-shift trend on heating due to the Bose-Einstein law. Moreover, the corresponding optical band gap E_g can be derived by the Tauc law: $(\alpha E)^n=A(E-E_g)$, here n=2 and 1/2 for direct and indirect materials, respectively. For the direct PMN-0.12PT ferroelectric materials, the band gap can be identified according the intercept of $(\alpha E)^2$ *vs.* E as shown in the inset of Figure 13.

In addition, Figure 14 shows the phase diagram of PMN-*x*PT based on the optical band gap derived by temperature and PT composition dependent transmittance spectra. It indicates a relationship between the band gap and phase transitions. Moreover, the experimental transmittance and corresponding absorbance can also directly probe structure variations of $NaBiTiO_3$-6%$BaTiO_3$ (NBT-6%BT) crystals directly [35]. Therefore, temperature-dependent transmittance spectroscopy is another effective tool to detect ferroelectric phase transitions nondestructively [91–93]. However, it is unsuitable for investigating opaque materials without optical band gap.

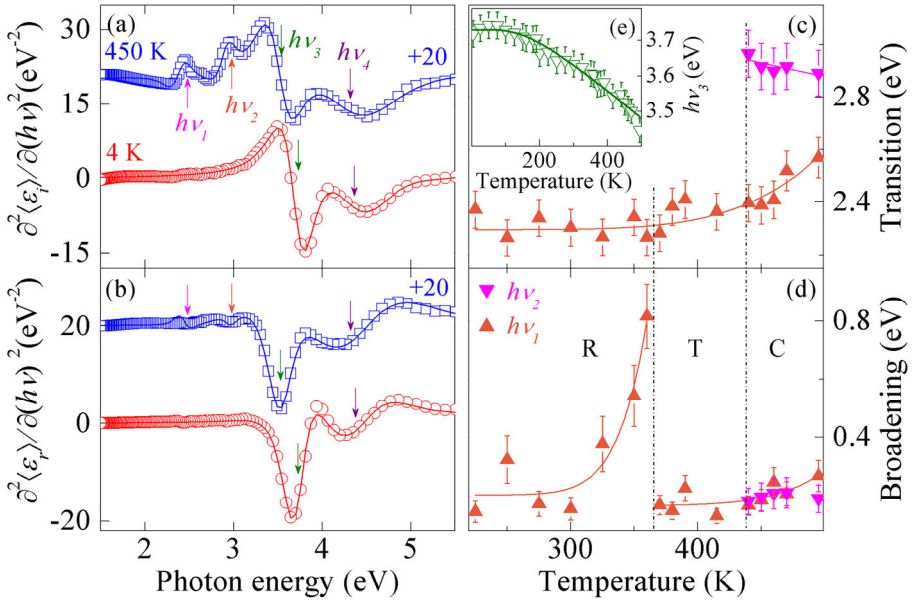

Figure 12 Experimental (dotted lines) and best-fitted (solid lines) second partial derivatives of the (a) imaginary $<\varepsilon_i>$ and (b) real $<\varepsilon_r>$ parts of pseudodielectric functions for PZN-7%PT single crystal at 4 and 450 K, respectively; (c) transition energies and (d) broadenings of $h\nu_1$ and $h\nu_2$ as a function of temperature; (e) temperature dependence of the transition energy (dotted lines) $h\nu_3$. The solid lines in (d) and (e) are the fitting results by the Bose-Einstein model [72].

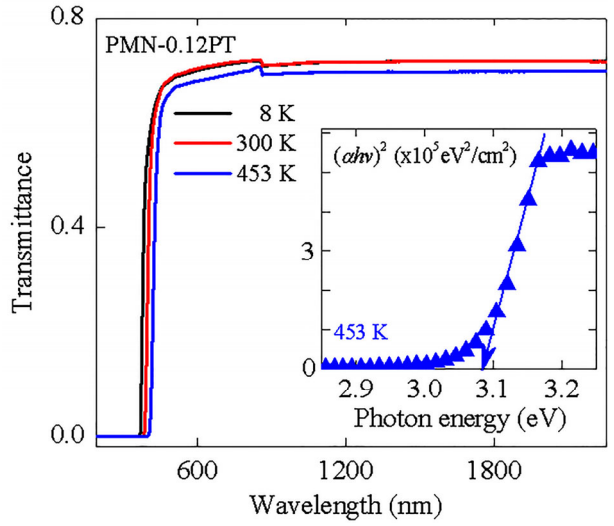

Figure 13 Temperature dependence of transmittance for PMN-0.12PT crystals and the inset is the function of $(ahv)^2$ as photon energy to determine the optical band gap [91].

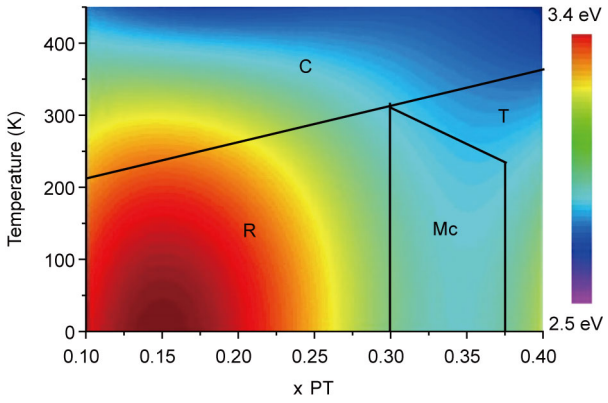

Figure 14 The phase diagram of PMN-*x*PT based on the optical band gap with various temperatures and PT compositions [91].

3.4 Photoluminescence spectroscopy

PL spectroscopy, which is another nondestructive, noncontact, and high sensitivity tool, is widely used to investigate photo-physical and photo-chemical properties of functional materials in optoelectronics and photo-catalysis fields. Moreover, the PL technique can supply much information such as lattice defects, surface/subsurface oxygen vacancies, as well as the separation and recombination of photo-induced charge carriers in amorphous, polycrystalline, and-crystal bulks and films [69,80]. Additional, the activation energy E_u for the thermal quenching process can be obtained according to temperature-dependent intensity I of PL emissions: $I=I_0/(1+ae^{Eu/kBT})$, where the parameter $a=\tau_R/\tau_0$ and τ_R is the radiative lifetime of electronic transitions from excited states to ground ones, and k_B is the Boltzmann's constant. Usually, PL spectroscopy is used as a diagnostic and development technique to develop electroluminescent devices such as light emitting lasers and diodes [94].

Figure 15(a) shows the experimental (dotted lines) and fitted (solid lines) PL spectrum of PMN-0.33PT crystals at 80 K. The emission E_a near 3.0 eV is ascribed to the optical band gap. It indicates a negative band gap narrowing trend due to lattice thermal expansion or renormalization of band structure by electron-phonon interaction (Figure 15(b)). The others (E_b, E_c, E_d, and E_e) are originated from bound states

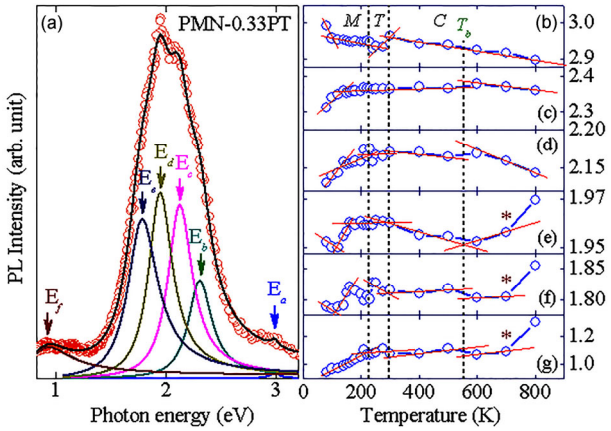

Figure 15 (Color online) (a) Deconvolution of the PL spectrum (solid line) for PMN-0.33PT crystals at 80 K and corresponding well-fitted emissions (b) E_a, (c) E_b, (d) E_c, (e) E_d, (f) E_e, and (g) E_f on heating. Note that the symbol "∗" marks the inflection point at 700 K [69].

within the band gap and have various behaviors with increasing the temperature as shown in Figure 15(c)–(g), respectively. The slightly abnormal trends at around 220 K come from the transition between M and T phases. Moreover, another transition temperature from T to C phases as well as the Burns temperature T_B are observed at about 300 and 550 K, respectively [69]. Therefore, PL is another condensed matter spectroscopy for detecting phase transitions of ferroelectric functional materials with lower electronic transition energies than that of the exciting laser.

4 Conclusion and prospect

In the review, we focus on detecting phase transitions of PT-based ferroelectric functional materials by using the condensed matter spectroscopic techniques such as SE, transmittance, PL as well as Raman scattering. Specifically, the temperature-dependent polarized Raman-active mode behaviors indicate that PZN-7%PT undergoes two phase transitions as well as an intermediate temperature upon heating. Moreover, phase diagrams of PIMN-*x*PT and PMN-*x*PT were sketched based on the various temperature responses of electronic transitions derived from ellipsometric and transmittance spectra, respectively. Compared to the traditional techniques (XRD, low frequency dielectric permittivity, etc.), optical techniques are nondestructive and noncontact, and can effectively supply much more information about physical and chemical properties (dielectric constant, optical band gap, electronic band structure, lattice dynamics, etc.) besides phase transitions and phase diagrams of ferroelectrics. In addition, it should be improve theoretically and experimentally as a novel technique for probing phase transitions in ferroelectric functional materials to overcome their disadvantages and limitations. At present, it is a better way to investigate phase transitions by combining traditional and novel techniques.

This work was supported by the Major State Basic Research Development Program of China (Grant No. 2013CB922300 & 2011CB922200), the National Natural Science Foundation of China (Grant Nos. 11374097, 61376129 & 61504156), the Projects of Science and Technology Commission of Shanghai Municipality (Grant Nos. 15JC1401600, 14XD1401500, 13JC1402100 & 13JC1404200), and the Program for Professor of Special Appointment (Eastern Scholar) at Shanghai Institutions of Higher Learning. The authors would like to thank Dr. ZHU JiaJun and ZHANG Xiao-Long for their valuable assistance in data acquisition.

1 Scott J F. Applications of modern ferroelectrics. Science, 2007, 315: 954–959
2 Moya X, Kar-Narayan S, Mathur N D. Caloric materials near ferroic phase transitions. Nat Mater, 2014, 13: 439–450
3 Zhang S J, Li F. High performance ferroelectric relaxor-$PbTiO_3$ single crystals: Status and perspective. J Appl Phys, 2012, 111: 031301
4 Wang Y J, Wang Z G, Ge W W, et al. Temperature-induced and electric-field-induced phase transitions in rhombohedral $Pb(In_{1/2}Nb_{1/2})O_3$-$Pb(Mg_{1/3}Nb_{2/3})O_3$-$PbTiO_3$ ternary single crystals. Phys Rev B, 2014, 90: 134107
5 Zhu J J, Li W W, Xu G S, et al. Abnormal temperature dependence of interband electronic transitions in relaxor-based ferroelectric $(1–x)Pb(Mg_{1/3}Nb_{2/3})O_3$-$xPbTiO_3$ (x=0.24 and 0.31) single crystals. Appl Phys Lett, 2011, 98: 091913
6 Auciello O, Scott J F, Ramesh R. The physics of ferroelectric memories. Phys Today, 1998, 51: 22–27
7 Spaldin N A, Cheong S W, Ramesh R. Multiferroics: Past, present, and future. Phys Today, 2010, 63: 38–43
8 Ahart M, Somayazulu M, Cohen R E, et al. Origin of morphotropic phase boundaries in ferroelectrics. Nature, 2008, 451: 545–548
9 Zhang S J, Li F, Jiang X N, et al. Advantages and challenges of relaxor-$PbTiO_3$ ferroelectric crystals for electroacoustic transducers-A review. Prog Mater Sci, 2015, 68: 1–66
10 Xu G S, Luo H S, Zhong W Z, et al. Morphology and defect structures of novel relaxor ferroelectric single crystals $Pb(Mg_{1/3}Nb_{2/3})O_3$-$PbTiO_3$. Sci China Tech Sci, 1999, 42: 541–549
11 Tang Y X, Shen Z Y, Zhang S J, et al. Minimization of pyroelectric effects in relaxor-$PbTiO_3$ crystals for piezoelectric sensors. Mater Chem Phys, 2014, 145: 135–140
12 Fang S X, Tang D Y, Chen Z M, et al. Elastic, dielectric, and piezoelectric characterization of $0.92Pb(Zn_{1/3}Nb_{2/3})O_3$-$0.08PbTiO_3$ single crystal by Brillouin scattering. Chin Phys B, 2015, 24: 027802
13 Srimathy B, Jayavel R, Ganesamoorthy S, et al. Crystal growth of PZN-PT single crystals and critical issues for higher piezoelectric coefficient. Cryst Res Tech, 2012, 47: 523–529
14 Xu G S, Luo H S, Xu H Q, et al. Third ferroelectric phase in PMNT single crystals near the morphotropic phase boundary composition. Phys Rev B, 2001, 64: 020102(R)
15 Kawamura S, Kaneko J H, Fujimoto H, et al. Possibility of using a PMN-PT single crystal as a neutron optical device. Phys B-Condens Matter, 2006, 385: 1277–1279
16 Singh A K, Pandey D, Zaharko O. Powder neutron diffraction study of phase transitions in and a phase diagram of $(1–x)[Pb(Mg_{1/3}Nb_{2/3})O_3]$-$xPbTiO_3$. Phys Rev B, 2006, 74: 024101
17 Phelan D, Rodriguez E E, Gao J, et al. Phase diagram of the relaxor ferroelectric $(1–x)Pb(Mg_{1/3}Nb_{2/3})O_3$-$xPbTiO_3$ revisited: A neutron powder diffraction study of the relaxor skin effect. Phase Transitions, 2015, 88: 283–305
18 Noheda B, Cox D E, Shirane G, et al. Phase diagram of the ferroelectric relaxor $(1–x)PbMg_{1/3}Nb_{2/3}O_3$-$xPbTiO_3$. Phys Rev B, 2002, 66: 054104
19 La-Orauttapong D, Noheda B, Ye Z G, et al. Phase diagram of the relaxor ferroelectric $(1–x)PbZn_{1/3}Nb_{2/3}O_3$-$xPbTiO_3$. Phys Rev B, 2002, 65: 144101
20 Barad Y, Lu Y, Cheng Z Y, et al. Composition, temperature, and crystal orientation dependence of the linear electro-optic properties of $Pb(Zn_{1/3}Nb_{2/3})O_3$-$PbTiO_3$ single crystals. Appl Phys Lett, 2000, 77: 1247–1249

21 Lu Y, Cheng Z Y, Barad Y, et al. Photoelastic effects in tetragonal $Pb(Zn_{1/3}Nb_{2/3})O_3$-$PbTiO_3$ single crystals near the morphotropic phase boundary. J Appl Phys, 2001, 89: 5075–5078

22 Akhilesh K S, Dhananjai P. Structure and the location of the morphotropic phase boundary region in $(1–x)[Pb(Mg_{1/3}Nb_{2/3})O_3]$-$xPbTiO_3$. J Phy-Condens Matter, 2001, 13: L931

23 Cox D E, Noheda B, Shirane G, et al. Universal phase diagram for high-piezoelectric perovskite systems. Appl Phys Lett, 2001, 79: 400–402

24 Jiang X P, Fang J W, Zeng H R, et al. Dielectric properties of $Pb(Zn_{1/3}Nb_{2/3})O_3$-$PbZrO_3$-$PbTiO_3$ solid solution near morphotropic phase boundary. Sci China Tech Sci, 2002, 45: 65–73

25 Xi Z, Bu Q, Fang P, et al. Effect of frequency and temperature on dielectric relaxation of [111]-oriented PMN-0.32PT single crystals. J Alloys Compd, 2015, 618: 14–18

26 He W, Li Q, Luo N, et al. Temperature and electric field induced phase transition in $[110]_C$-oriented $0.63Pb(Mg_{1/3}Nb_{2/3})O_3$-$0.37PbTiO_3$ single crystals. Cryst Eng Comm, 2015, 17: 8664–8670

27 Wan Y H, Li Z R, Ma M, et al. Dielectric behavior and phase transition in [111]-oriented PIN-PMN-PT single crystals under dc bias. J Adv Dielect, 2014, 04: 1450004

28 Lu Y, Jeong D Y, Cheng Z Y, et al. Phase transitional behavior and piezoelectric properties of the orthorhombic phase of $Pb(Mg_{1/3}Nb_{2/3})O_3$-$PbTiO_3$ single crystals. Appl Phys Lett, 2001, 78: 3109–3111

29 Han J P, Cao W W. Electric field effects on the phase transitions in [001]-oriented $(1–x)Pb(Mg_{1/3}Nb_{2/3})O_3$-$xPbTiO_3$ single crystals with compositions near the morphotropic phase boundary. Phys Rev B, 2003, 68: 134102

30 Zekria D, Shuvaeva V A, Glazer A M. Birefringence imaging measurements on the phase diagram of $Pb(Mg_{1/3}Nb_{2/3})O_3$-$PbTiO_3$. J Phys-Condens Matter, 2005, 17: 1593

31 Lin D B, Li Z R, Li F, et al. Direct observation of domain wall motion and novel dielectric loss in $0.23Pb(In_{1/2}Nb_{1/2})O_3$-0.42Pb $(Mg_{1/3}Nb_{2/3})O_3$-$0.35PbTiO_3$ crystals. Cryst Eng Comm, 2013, 15: 6292–6296

32 Zheng L M, Lu X Y, Shang H S, et al. Hysteretic phase transition sequence in $0.67Pb(Mg_{1/3}Nb_{2/3})O_3$-$0.33PbTiO_3$ single crystal driven by electric field and temperature. Phys Rev B, 2015, 91: 06412

33 Li Q, Liu Y, Wang J, et al. Structural transitions in [001]/[111]-oriented $0.26Pb(In_{1/2}Nb_{1/2})O_3$-$0.46Pb(Mg_{1/3}Nb_{2/3})O_3$-$0.28PbTiO_3$ single crystals probed via neutron diffraction and electrical characterization. J Appl Phys, 2013, 113: 154104

34 Xu L P, Jiang K, Zhang J Z, et al. Phase transitions and thermotropic phase boundaries in MnO_2-doped $(K_{0.5}Na_{0.5})NbO_3$-$0.05LiNbO_3$ single crystals: Raman scattering evidence at elevated temperatures. Appl Phys Lett, 2015, 106: 122901

35 Huang T, Hu Z G, Xu G S, et al. Inherent optical behavior and structural variation in $Na_{0.5}Bi_{0.5}TiO_3$-6%$BaTiO_3$ revealed by temperature dependent Raman scattering and ultraviolet-visible transmittance. Appl Phys Lett, 2014, 104: 111908

36 Chen X, Hu Z G, Duan Z H, et al. Effects from a-site substitution on morphotropic phase boundary and phonon modes of $(Pb_{1–1.5x}La_x)(Zr_{0.42}Sn_{0.40}Ti_{0.18})O_3$ ceramics by temperature dependent Raman spectroscopy. J Appl Phys, 2013, 114: 043507–043505

37 Chen C, Deng H, Li X B, et al. Study of field-induced phase transitions in $0.68PbMg_{1/3}Nb_{2/3}O_3$-$0.32PbTiO_3$ relaxor single crystal by polarized micro-Raman spectroscopy. Appl Phys Lett, 2014, 105: 102909

38 Slodczyk A, Daniel P, Kania A. Local phenomena of $(1–x)Pb\ Mg_{1/3}Nb_{2/3}O_3$-$xPbTiO_3$ single crystals ($0 \le x \le 0.38$) studied by Raman scattering. Phys Rev B, 2008, 77: 184114

39 Joya M R, Barón-Jaimez J, Barba-Ortega J. The technique of Raman spectroscopy in the characterization physical, chemical and structural ferroelectric of the materials. J Phys-Conf Ser, 2013, 466: 012007

40 Cheng J, Yang Y, Tong Y H, et al. Study of monoclinic-tetragonal-cubic phase transition in $Pb(Zn_{1/3}Nb_{2/3})O_3$-$0.08PbTiO_3$ single crystals by micro-Raman spectroscopy. J Appl Phys, 2009, 105: 053519

41 Dorywalski K, Andriyevsky B, Piasecki M, et al. Structural phase transitions in ferroelectric crystals and thin films studied by VUV spectroscopic ellipsometry with synchrotron radiation. Phase Transitions, 2013, 86: 932–940

42 Katzke H, Dietze M, Lahmar A, et al. Dielectric, ultraviolet/visible, and Raman spectroscopic investigations of the phase transition sequence in $0.71Pb(Mg_{1/3}Nb_{2/3})O_3$-$0.29PbTiO_3$ crystals. Phys Rev B, 2011, 83: 174115

43 Deyneka A, Suchaneck G, Jastrabik L, et al. Phase transition shift in lead-excess PZT films under UV illumination. Integr Ferroelectr, 2004, 67: 173–180

44 Jiang P P, Duan Z H, Xu L P, et al. Phase transformation in multiferroic $Bi_5Ti_3FeO_{15}$ ceramics by temperature-dependent ellipsometric and Raman spectra: An interband electronic transition evidence. J Appl Phys, 2014, 115: 083101

45 Kamba S, Buixaderas E, Petzelt J, et al. Infrared and Raman spectroscopy of $[Pb(Zn_{1/3}Nb_{2/3})O_3]_{0.92}$-$[PbTiO_3]_{0.08}$ and $[Pb(Mg_{1/3}Nb_{2/3})O_3]_{0.71}$-$[PbTiO_3]_{0.29}$ single crystals. J Appl Phys, 2003, 93: 933–939

46 Kesavamoorthy R, Sivasubramanian V. Core-shell nanostructure and its phase transitions in $Pb(Mg_{1/3}Nb_{2/3})O_3$ by Raman spectroscopy and photoluminescence. J Raman Spectrosc, 2007, 38: 762–769

47 David W I F, Shankland K. Structure determination from powder diffraction data. Acta Crystallogr Sect A-Found Crystallogr, 2008, 64: 52–64

48 Bai F M, Wang N G, Li J F, et al. X-ray and neutron diffraction investigations of the structural phase transformation sequence under electric field in $0.7Pb(Mg_{1/3}Nb_{2/3})$-$0.3PbTiO_3$ crystal. J Appl Phys, 2004, 96: 1620–1627

49 Singh B K, Kumar K, Sinha N, et al. Flux growth and low temperature dielectric relaxation in piezoelectric $Pb[(Zn_{1/3}Nb_{2/3})_{0.91}Ti_{0.09}]O_3$ single crystals. Cryst Res Tech, 2009, 44: 915–924

50 Zhang Y Y, Li X B, Liu D A, et al. The compositional segregation, phase structure and properties of $Pb(In_{1/2}Nb_{1/2})O_3$-$Pb(Mg_{1/3}Nb_{2/3})O_3$-$PbTiO_3$ single crystal. J Cryst Growth, 2011, 318: 890–894

51 Wang Z J, Li X Z, Long X F, et al. Characterization of relaxor ferroelectric behavior in the $(1–x)Ba(Yb_{1/2}Nb_{1/2})O_3$-$xPbTiO_3$ solid solution. Scripta Mater, 2009, 60: 830–833

52 Tu C S, Schmidt V H, Shih I C, et al. Phase transformation via a monoclinic phase in relaxor-based ferroelectric crystal $(PbMg_{1/3}Nb_{2/3}O_3)_{1–x}(PbTiO_3)_x$. Phys Rev B, 2003, 67: 020102(R)

53 Li F, Zhang S J, Xu Z, et al. Critical property in relaxor-$PbTiO_3$ single crystals-shear piezoelectric response. Adv Funct Mater, 2011, 21: 2118–2128

54 Li F, Zhang S J, Xu Z, et al. Temperature independent shear piezoelectric response in relaxor-$PbTiO_3$ based crystals. Appl Phys Lett, 2010, 97: 252903

55 Duan Z H, Chang P, Hu Z G, et al. Temperature dependent Raman scattering and far-infrared reflectance spectra of MgO modified $Pb_{0.99}(Zr_{0.95}Ti_{0.05})_{0.98}Nb_{0.02}O_3$ ceramics: A composition effect. J Appl Phys, 2014, 116: 093513

56 Jiang P P, Zhang X L, Chang P, et al. Spin-phonon interactions of multiferroic $Bi_4Ti_3O_{12}$-$BiFeO_3$ ceramics: Low-temperature Raman scattering and infrared reflectance spectra investigations. J Appl Phys, 2014, 115: 144101

57 Xu L P, Zhang L L, Zhang X L, et al. Phase transformations in multiferroic $Bi_{1–x}La_xFe_{1–y}Ti_yO_3$ ceramics probed by temperature dependent Raman scattering. J Appl Phys, 2014, 116: 164103

58 Chen C, Zhang H W, Deng H, et al. Electric field and temperature-induced phase transition in Mn doped $Na_{1/2}Bi_{1/2}TiO_3$-5.0at.% $BaTiO_3$ single crystals investigated by micro-Raman scattering. Appl Phys Lett, 2014, 104: 142902

59 Ding X J, Xu L P, Hu Z G, et al. Phase diagram and incommensurate antiferroelectric structure in $(Pb_{1–1.5x}La_x)(Zr_{0.42}Sn_{0.40}Ti_{0.18})O_3$ ceramics discovered by band-to-band optical transitions. Appl Phys Lett, 2014, 105: 131909

60 Duan Z H, Jiang K, Xu L P, et al. Intrinsic relationship between electronic structures and phase transition of $SrBi_{2–x}Nd_xNb_2O_9$ ceramics from ultraviolet ellipsometry at elevated temperatures. J Appl Phys, 2014, 115: 054107

61 Duan Z H, Hu Z G, Jiang K, et al. Temperature-dependent dielectric functions and interband critical points of relaxor lead haf-

nate-modified $PbSc_{1/2}Ta_{1/2}O_3$ ferroelectric ceramics by spectroscopic ellipsometry. Appl Phys Lett, 2013, 102: 151908
62 Chen X, Jiang P P, Duan Z H, et al. The a-site driven phase transition procedure of $(Pb_{0.97}La_{0.02})$ $(Zr_{0.42}Sn_{0.40}Ti_{0.18})O_3$ ceramics: An evidence from electronic structure variation. Appl Phys Lett, 2013, 103: 192910
63 Xu L P, Zhang L L, Jiang P P, et al. Interband electronic transitions and phase transformation of multiferroic $Bi_{1-x}La_xFe_{1-y}Ti_yO_3$ ceramics revealed by temperature-dependent spectroscopic ellipsometry. J Appl Phys, 2013, 114: 233509
64 Huang T, Guo S, Xu L P, et al. Low temperature structural variations of $Na_{0.5}Bi_{0.5}TiO_3$-7%$BaTiO_3$ single crystal: Evidences from optical ellipsometry and Raman scattering. J Appl Phys, 2015, 117: 224103
65 Deyneka A, Suchaneck G, Hubicka Z, et al. Ellipsometry of high temperature phase transitions in PZT and (ZnLi)O films. Ferroelectrics, 2004, 298: 55–60
66 Tyunina M, Dejneka A, Chvostova D, et al. Phase transitions in ferroelectric $Pb_{0.5}Sr_{0.5}TiO_3$films probed by spectroscopic ellipsometry. Phys Rev B, 2012, 86: 224105
67 Dejneka A, Zablotskii V, Tyunina M, et al. Ellipsometry applied to phase transitions and relaxation phenomena in Ni_2MnGa ferromagnetic shape memory alloy. Appl Phys Lett, 2012, 101: 141908
68 Zhu J J, Zhang J Z, Xu G S, et al. UV-Vis-NIR optical properties of $Pb(Mg_{1/3}Nb_{2/3})O_3$-0.3$PbTiO_3$ single crystal. J Infrared Millim Waves, 2015, 34: 442–446
69 Zhang X L, Zhu J J, Zhang J Z, et al. Photoluminescence study on polar nanoregions and structural variations in $Pb(Mg_{1/3}Nb_{2/3})O_3$-$PbTiO_3$ single crystals. Opt Express, 2014, 22: 21903
70 Khanna R K, Stranz D D, Donn B. A spectroscopic study of intermediates in the condensation of refractory smokes: Matrix isolation experiments of SiO. J Chem Phys, 1981, 74: 2108–2115
71 Zhu J J, Zhang J Z, Xu G S, et al. Phonon modes and local polar distortions in nanoclusters of $Pb(In_{1/2}Nb_{1/2})O_3$-$Pb(Mg_{1/3}Nb_{2/3})O_3$-$PbTiO_3$ crystals probed by terahertz reflectance spectra and Raman scattering. Laser Phys Lett, 2015, 12: 056103
72 Zhang J Z, Tong W Y, Zhu J J, et al. Temperature-dependent lattice dynamics and electronic transitions in 0.93$Pb(Zn_{1/3}Nb_{2/3})O_3$-0.07$PbTiO_3$ single crystals: Experiment and theory. Phys Rev B, 2015, 91: 085201
73 Zhu J J, Jiang K, Xu G S, et al. Temperature-dependent Raman scattering and multiple phase coexistence in relaxor ferroelectric $Pb(In_{1/2}Nb_{1/2})O_3$-$Pb(Mg_{1/3}Nb_{2/3})O_3$-$PbTiO_3$ single crystals. J Appl Phys, 2013, 114: 153508
74 Dubroka A, Humlíček J, Abrashev M V, et al. Raman and infrared studies of $La_{1-y}Sr_yMn_{1-x}M_xO_3$ (M=Cr, Co, Cu, Zn, Sc or Ga): Oxygen disorder and local vibrational modes. Phys Rev B, 2006, 73: 224401
75 Waeselmann N, Maier B J, Mihailova B, et al. Pressure-induced structural transformations in pure and Ru-doped 0.9$PbZn_{1/3}Nb_{2/3}O_3$-0.1$PbTiO_3$ near the morphotropic phase boundary. Phys Rev B, 2012, 85: 014106
76 Svitelskiy O, La-Orauttapong D, Toulouse J, et al. $PbTiO_3$ addition and internal dynamics in $Pb(Zn_{1/3}Nb_{2/3})O_3$ crystal studied by Raman spectroscopy. Phys Rev B, 2005, 72: 172106
77 Dobal P S, Katiyar R S, Tu C S. Study of ordered nano-regions in $Pb(Zn_{1/3}Nb_{2/3})_{0.915}Ti_{0.085}O_3$ single crystal using Raman spectroscopy. J Raman Spectrosc, 2003, 34: 152–156
78 Zhang X L, Zhu J J, Xu G S, et al. Temperature dependent spectroscopic ellipsometry and Raman scattering of $PbTiO_3$-based relaxor ferroelectric single crystals around MPB region. Opt Mater Express, 2015, 5: 2478–2490
79 Zhang J Z, Shen Y D, Li Y W, et al. Composition dependence of microstructure, phonon modes, and optical properties in rutile TiO_2:Fe nanocrystalline films prepared by a nonhydrolytic Sol-Gel route. J Phys Chem C, 2010, 114: 15157–15164
80 Zhang J Z, Chen X G, Shen Y D, et al. Synthesis, surface morphology, and photoluminescence properties of anatase iron-doped titanium dioxide nano-crystalline films. Phys Chem Chem Phys, 2011, 13: 13096–13105
81 Zhang J Z, Chen X G, Jiang K, et al. Evolution of orientation degree, lattice dynamics and electronic band structure properties in nano-crystalline lanthanum-doped bismuth titanate ferroelectric films by chemical solution deposition. Dalton Trans, 2011, 40: 7967–7975
82 Zhang J Z, Zhu J J, Deng Q L, et al. The optical properties of La doped $BiGaO_3$ polycrystalline films. J Infrared Millm Waves, 2015, 34: 447–451
83 Azzam R M A, Bashara N M. Ellipsometry and Polarized Light. Amsterdam: North-Holland Publishing Company, 1977
84 Djurišić A B, Chan Y, Herbert L E. Progress in the room temperature optical functions of semiconductors. Mater Sci Eng R, 2002, 38: 237–293
85 Fujiwara H, Koh J, Rovira P I, et al. Assessment of effective-medium theories in the analysis of nucleation and microscopic surface roughness evolution for semiconductor thin films. Phys Rev B, 2000, 61: 10832
86 Lautenschlager P, Garriga M, Vina L, et al. Temperature dependence of the dielectric function and interband critical points in silicon. Phys Rev B, 1987, 36: 4821–4830
87 Lee H, Kang Y S, Cho S J, et al. Dielectric functions and electronic band structure of lead zirconate titanate thin films. J Appl Phys, 2005, 98: 094108
88 Suewattana M, Singh D J. Electronic structure and lattice distortions in $PbMg_{1/3}Nb_{2/3}O_3$ studied with density functional theory using the linearized augmented plane-wave method. Phys Rev B, 2006, 73: 224105
89 Wang D W, Cao M S, Zhang S J. Phase diagram and properties of $Pb(In_{1/2}Nb_{1/2})O_3$-$Pb(Mg_{1/3}Nb_{2/3})O_3$-$PbTiO_3$ polycrystalline ceramics. J Eur Ceram Soc 2012, 32: 433–439
90 Xu G S, Chen K, Yang D F, et al. Growth and electrical properties of large size $Pb(In_{1/2}Nb_{1/2})O_3$-$Pb(Mg_{1/3}Nb_{2/3})O_3$-$PbTiO_3$ crystals prepared by the vertical Bridgman technique. Appl Phys Lett, 2007, 90: 032901
91 Zhang X L, Hu Z G, Xu G S, et al. Optical bandgap and phase transition in relaxor ferroelectric $Pb(Mg_{1/3}Nb_{2/3})O_3$-$x$$PbTiO_3$ single crystals: An inherent relationship. Appl Phys Lett, 2013, 103: 051902
92 Zhu J J, Li W W, Xu G S, et al. A phenomenological model of electronic band structure in ferroelectric $Pb(In_{1/2}Nb_{1/2})O_3$-$Pb(Mg_{1/3}Nb_{2/3})O_3$-$PbTiO_3$ single crystals around the morphotropic phase boundary determined by temperature-dependent transmittance spectra. Acta Mater, 2011, 59: 6684–6690
93 Zhu J J, Zhang J Z, Xu G S, et al. Electronic transitions and dielectric functions of relaxor ferroelectric $Pb(In_{1/2}Nb_{1/2})O_3$-$Pb(Mg_{1/3}Nb_{2/3})O_3$-$PbTiO_3$ single crystals: Temperature dependent spectroscopic study. Appl Phys Lett, 2014, 104: 132903
94 Fan Z Y, Chang P C, Lu J G, et al. Photoluminescence and polarized photodetection of single ZnO nanowires. Appl Phys Lett, 2004, 85: 6128–6130